Pseudo-Critical Inlet State Mapping of an sCO_2-Water Printed Circuit Heat Exchanger Pre-Cooler for Brayton Cycles

Ory Haimovitz, Independent Researcher, Haifa, Israel

Corresponding Author: ory.haimo@gmail.com

Abstract

A design-oriented inlet state mapping methodology is presented for a printed circuit heat exchanger (PCHE) operating as a supercritical carbon dioxide (sCO_2) water pre-cooler in a Brayton-cycle application. The objective is to quantify how the thermal and hydraulic response of a fixed straight-channel PCHE core changes as the sCO_2 inlet state moves relative to the pseudo-critical region. A one-dimensional distributed counterflow model is formulated for a representative hot-side and cold-side channel pair. Real-fluid thermophysical properties are evaluated locally from pressure and specific enthalpy, and local heat-transfer and friction models are coupled with a wall conduction resistance represented through a two-dimensional conduction shape factor. The boundary-value problem is solved using a shooting method.

The model is assessed against straight channel sCO_2-water PCHE data from the literature. For four outlet temperature comparison cases, the mean absolute error is approximately 0.6 K for the CO_2 outlet temperature and 1.28 K for the water outlet temperature. An additional comparison with digitized near critical axial temperature profiles is treated as a profile shape consistency check.

The assessed model is applied to a fixed semicircular channel PCHE geometry over maps of hot side inlet pressure and temperature for three cooling water inlet temperatures. The maps show heat duty, effectiveness, straight core pressure drop, mean overall heat-transfer coefficient, minimum temperature approach, and hot outlet temperature. The results demonstrate the competing influence of pseudo-critical heat transfer enhancement, heat sink temperature, pinch margin, and hydraulic penalty, providing a compact preliminary design tool for sCO_2 Brayton cycle pre-cooler assessment.

Keywords: supercritical carbon dioxide; printed circuit heat exchanger; pre-cooler; pseudo-critical region; Brayton cycle; state mapping; real-fluid heat transfer

1. Introduction

Supercritical carbon dioxide (sCO_2) Brayton cycles have attracted sustained attention for advanced power conversion systems because they can combine high thermodynamic efficiency, compact equipment, and compatibility with nuclear, solar-thermal, geothermal, and waste heat recovery heat sources [1-3]. A principal advantage of these cycles is that compression can be performed close to the critical region, where the density of CO_2 is high and the compression work can be reduced. This advantage also makes the cycle sensitive to the thermal state delivered to the compressor. Consequently, the pre-cooler directly influences compressor-inlet conditions, operating stability, and cycle performance [2,3].

Printed circuit heat exchangers (PCHEs) are widely considered strong candidates for sCO_2 Brayton-cycle applications because they offer high compactness, high pressure resistance, and good heat-transfer performance [3-5]. PCHEs are commonly manufactured by photochemical etching of small channels into metal plates, followed by diffusion bonding to form a compact monolithic core. Compared with conventional shell-and-tube heat exchangers, PCHEs provide higher area density and improved suitability for high pressure operation, making them attractive for recuperators, primary heat exchangers, and pre-coolers in sCO_2 systems [3-5].

The pre-cooler is a particularly demanding PCHE application because the sCO_2 stream is cooled near the critical or pseudo-critical region. In this region, thermophysical properties such as specific heat, density, viscosity, and thermal conductivity vary strongly with temperature and pressure. These property variations affect local heat transfer coefficients, pressure drop, temperature approach, and outlet-state prediction. Therefore, average property or lumped heat-exchanger models may be inadequate when the CO_2 thermal trajectory approaches or crosses the pseudo-critical region [7,10,13]. Distributed models with state-dependent property evaluation are better suited to this problem because they can resolve the axial variation of fluid state and transport properties.

Previous studies have provided important experimental and numerical information on sCO_2 cooling in PCHEs. Chu et al. [6] experimentally investigated sCO_2-water heat transfer in a straight-channel PCHE and examined the influence of pressure and the pseudo-critical region on thermal-hydraulic performance. Ren et al. [7] studied local convective heat transfer during cooling of sCO_2 in horizontal semicircular PCHE channels and developed correlations that account for strong thermophysical-property variation and buoyancy effects. Li et al. [8] proposed a working point-based method to evaluate overall heat-transfer performance of sCO_2 in a PCHE. Cheng et al. [9] experimentally investigated a 100 kW-class PCHE used as a pre-cooler for an sCO_2 Brayton cycle. Park et al. [10] emphasized the need for careful data treatment in near-critical sCO_2-water PCHE experiments, and Liu et al. [11] combined experiments and CFD simulations for a straight-channel PCHE pre-cooler. More recent work has extended available cooling data for alternative PCHE channel configurations [12].

Although these studies have substantially improved understanding of sCO_2 cooling in PCHEs, many results are reported as individual operating points, local heat-transfer behavior, empirical correlations, or conventional parametric trends. For preliminary design, however, it is useful to know how a fixed PCHE pre-cooler geometry responds over a two-dimensional range of possible inlet states. A designer must often evaluate heat duty, effectiveness, pressure drop, outlet temperature, minimum temperature approach, and heat-transfer enhancement simultaneously. The operating point that maximizes heat duty is not necessarily the point that maximizes effectiveness, minimizes pressure drop, or gives the desired compressor-inlet temperature.

The present work develops a design-oriented inlet-state mapping methodology for an sCO_2-water PCHE pre-cooler. A one-dimensional distributed counterflow model is formulated with real-fluid thermophysical properties, local heat transfer and friction models, and a wall conduction resistance represented through a conduction shape factor. The model is first compared with experimental outlet-temperature data from the literature for a straight-channel PCHE pre-cooler. It is then applied to a fixed straight semicircular-channel PCHE geometry over a two-dimensional map of hot-side inlet

pressure and hot-side inlet temperature. The pseudo-critical line is superimposed on the maps to distinguish liquid-like and gas-like supercritical inlet regions, while three water inlet temperatures are considered to quantify the influence of heat-sink temperature.

The intended contribution is not a new heat transfer correlation or a full component-level PCHE design tool. Rather, the contribution is a compact pseudo-critical state-map framework that connects distributed real-fluid pre-cooler calculations with early-stage design interpretation. Within the limits of the selected geometry, correlations, and validation data, the maps identify how cooling capacity, effectiveness, straight-core pressure loss, minimum temperature approach, heat transfer enhancement, and hot outlet temperature vary as the inlet state moves relative to the pseudo-critical region.

2. Model description

A one-dimensional distributed model was developed to predict the thermal-hydraulic response of a PCHE operating as an sCO_2-water pre-cooler. The exchanger core is represented by one repeated hot-side and cold-side channel pair arranged in counterflow. This representative-channel approach is appropriate for a periodically repeated straight-channel PCHE core when the parallel channels are assumed to be geometrically identical and to receive uniform flow distribution. The model is therefore a core-channel model; it does not resolve headers, manifolds, port regions, flow maldistribution, or entrance and exit losses.

The hot fluid is sCO_2 and the cold fluid is water. Both fluids are treated as real fluids, and local thermophysical properties are evaluated from pressure and specific enthalpy using CoolProp [14], which is based on established equations of state, including the Span-Wagner formulation for CO_2 [15]. The axial coordinate $x$is measured from the hot-side inlet to the hot-side outlet. Because the exchanger is operated in counterflow, the cold-side flow direction is opposite to the positive x-direction.

2.1. Geometry and distributed balances

For a semicircular channel of diameter D, the cross-sectional area, wetted perimeter, hydraulic diameter, and heat transfer area of one representative channel are

$$A_c = \frac{\pi D^2}{8}, \tag{1}$$

$$P_w = D\left(1+\frac{\pi}{2}\right), \tag{2}$$

$$D_h = \frac{4A_c}{P_w} = \frac{\pi D}{\pi + 2}, \tag{3}$$

$$A_h = P_w L. \tag{4}$$

The heat transfer rate per unit length is:

$$q'(x) = U(x)P_w[T_h(x) - T_c(x)], \tag{5}$$

where $U(x)$is the local overall heat-transfer coefficient. The distributed enthalpy balances are

$$\frac{dh_h}{dx} = -\frac{q'(x)}{\dot{m}_h}, \qquad (6)$$

$$\frac{dh_c}{dx} = -\frac{q'(x)}{\dot{m}_c}. \qquad (7)$$

Here, $\dot{m}_h$and $\dot{m}_c$are the hot- and cold-side mass flow rates per channel. The negative sign in Eq. (7) follows from using the hot-side flow direction as the positive coordinate while the cold stream flows in the opposite direction.

2.2. Heat-transfer, wall-resistance, and pressure-drop models

The local overall heat-transfer coefficient is evaluated from a series thermal-resistance model,

$$\frac{1}{U(x)} = \frac{1}{h_h(x)} + R_w + \frac{1}{h_c(x)}, \qquad (8)$$

where h_h and h_c are the local hot- and cold-side convective heat-transfer coefficients, respectively, and R_w is the wall conduction resistance expressed per unit heat-transfer area.

Several published sCO_2-side heat-transfer correlations were implemented and tested during model development, including correlations based on Ren et al. [7], Liu et al. [11], a Gnielinski-type formulation, and limiting constant-Nusselt-number forms. The final calculations use the Ren et al. [7] correlation for cooling of sCO_2 in horizontal semicircular PCHE channels. This choice was made because the correlation was developed for a geometry and cooling process close to the present application and provided the most consistent agreement with the available validation data without re-fitting empirical coefficients. The optional entrance correction was not applied in the present calculations, so that the same closure could be used consistently for the validation cases and state-map calculations.

The water-side heat transfer coefficient is evaluated using the Gnielinski correlation [16],

$$Nu = \frac{(f/8)(Re - 1000)Pr}{1 + 12.7(f/8)^{1/2}\left(Pr^{2/3} - 1\right)}, \qquad (9)$$

where f is the Darcy friction factor. The same water-side closure was used for all validation and state-map calculations. Since water properties vary only weakly over the present temperature range compared with sCO_2 near the pseudo-critical region, the dominant heat-transfer closure uncertainty is expected to arise from the sCO_2 side.

At each axial location, the wall temperature is obtained iteratively because the sCO_2 heat-transfer correlation depends on property ratios evaluated at bulk and wall temperatures. The wall-side iteration is performed locally until the change in wall temperature falls below the specified tolerance. This treatment is important near the pseudo-critical region, where density, viscosity, thermal conductivity, and specific heat can vary strongly over small temperature intervals.

The wall conduction resistance is represented by a dimensionless two-dimensional conduction shape factor, S, computed separately for the PCHE unit-cell geometry. The corresponding resistance used by the one-dimensional model is:

$$R_w = \frac{P_w}{k_w S}, \qquad (10)$$

where k_w is the wall thermal conductivity. This approach allows the distributed one-dimensional model to include the first-order influence of transverse solid conduction without solving a two-dimensional conduction problem at every operating point.

The straight-channel pressure drop is calculated from a local one-dimensional momentum balance. The frictional components are written as:

$$\frac{dp_h}{dx} = -\frac{f_h(x) G_h^2}{2\rho_h(x) D_h}, \qquad (11)$$

$$\frac{dp_c}{dx} = +\frac{f_c(x) G_c^2}{2\rho_c(x) D_h}, \qquad (12)$$

where the sign convention in Eq. (12) follows from measuring $x$in the hot-side flow direction. The mass flux is:

$$G = \frac{\dot{m}}{A_c}. \qquad (13)$$

Here, ρ is the local density, D_h is the hydraulic diameter, and f is the Darcy friction factor. In the present calculations, the Filonenko smooth-channel friction correlation [18] is used,

$$f = [1.82\log_{10}(Re) - 1.64]^{-2}, \qquad (14)$$

with the local Reynolds number evaluated from the local viscosity. The acceleration pressure-drop contribution associated with axial density variation is also included in the differential momentum equation. The reported pressure drops correspond to straight-core channel losses only. Header losses, inlet contraction, outlet expansion, port losses, and flow maldistribution are not included and are therefore outside the validation scope of the present model.

2.3. Numerical solution and performance quantities

The governing equations form a two-point boundary-value problem because the hot-side inlet state is prescribed at $x = 0$, whereas the cold-side inlet state is prescribed at $x = L$. The problem is solved using a shooting method. The unknown cold-side outlet state at $x = 0$, represented by the cold-side outlet enthalpy and pressure, is treated as the shooting variable. For a trial cold-side outlet state, the coupled energy and pressure equations are integrated from $x = 0$ to $x = L$. The trial values are then adjusted until the calculated cold-side state at $x = L$ matches the prescribed cold-side inlet enthalpy and pressure.

For numerical stability, pressure is integrated using a logarithmic pressure variable,

$$z = \ln\left(\frac{p}{p_{\mathrm{in}}}\right), \qquad (15)$$

so that pressure remains positive during the nonlinear iteration. The state vector used in the axial integration is therefore:

$$\mathbf{y}(x) = [h_h(x), z_h(x), h_c(x), z_c(x)]^T. \qquad (16)$$

The residual vector for the shooting method is defined from the mismatch between the calculated and prescribed cold-side inlet state at $x = L$,

$$\mathbf{R} = \left[\frac{h_c(L) - h_{c,\mathrm{in}}}{h_{\mathrm{scale}}}, z_c(L) - z_{c,\mathrm{in}}\right]^T, \qquad (17)$$

where h_{scale} is an enthalpy scale used for normalization. The nonlinear system $\mathbf{R} = \mathbf{0}$ is solved using a root-finding algorithm. The axial integration itself is performed with an adaptive Runge-Kutta method using fixed relative and absolute tolerances. At each integration point, thermophysical properties are evaluated from the local pressure and specific enthalpy, and the local wall temperature is iterated before evaluating the heat-transfer coefficients.

After convergence, the heat duty per representative channel is calculated from the hot-side enthalpy change,

$$Q_{\mathrm{ch}} = \dot{m}_h\left(h_{h,\mathrm{in}} - h_{h,\mathrm{out}}\right), \qquad (18)$$

and checked against the cold-side enthalpy gain,

$$Q_{\mathrm{ch},c} = \dot{m}_c\left(h_{c,\mathrm{out}} - h_{c,\mathrm{in}}\right). \qquad (19)$$

The heat-exchanger effectiveness is defined on an enthalpy basis,

$$\varepsilon = \frac{Q_{\mathrm{ch}}}{Q_{\mathrm{max}}}, \qquad (20)$$

with:

$$Q_{\mathrm{max}} = \min\left[\dot{m}_h\left(h_{h,\mathrm{in}} - h_h(T_{c,\mathrm{in}}, p_{h,\mathrm{in}})\right), \dot{m}_c\left(h_c(T_{h,\mathrm{in}}, p_{c,\mathrm{in}}) - h_{c,\mathrm{in}}\right)\right]. \qquad (21)$$

This real-fluid definition avoids using constant heat-capacity assumptions near the pseudo-critical region. It is used as a design-oriented comparison metric between map points; pressure-drop effects are not included in the ideal limiting heat duty.

The minimum local temperature approach is evaluated from the distributed solution as

$$\Delta T_{\min} = \min_{x} [T_h(x) - T_c(x)]. \qquad (22)$$

The integrated conductance is calculated as

$$UA = \int_0^L U(x)\, P_w\, dx, \qquad (23)$$

and the mean overall heat-transfer coefficient is

$$\bar{U} = \frac{UA}{A_h}. \qquad (24)$$

The active-core volumetric heat duty is reported as

$$q'''_{\text{core}} = \frac{Q_{\text{total}}}{V_{\text{core}}}. \qquad (25)$$

The same numerical procedure is used for all validation cases and for all points in the two-dimensional inlet-state maps. In the state-map calculations, the geometry, wall properties, channel count, and mass flow rates are fixed, while the hot-side inlet pressure and temperature are varied. Each map point is solved independently; previously converged neighboring points are used only as initial guesses to improve robustness and computational efficiency.

3. Model assessment and consistency checks

The one-dimensional distributed model was assessed against two experimental datasets for straight-channel sCO_2- water printed circuit heat exchangers operating under pre-cooler conditions. The first comparison uses outlet-temperature data reported by Liu et al. [11], whereas the second comparison uses distributed temperature profiles reported by Park et al. [10] for a near-critical cooling case. These two comparisons serve different purposes. The Liu et al. comparison is used as the primary outlet-temperature assessment because the required inlet and outlet quantities are available. The Park et al. comparison is used only as an axial profile-shape consistency check, since the mass flow rate corresponding to the selected plotted temperature-profile case was not explicitly available and was therefore inferred from the thermal response.

The comparison with Liu et al. [11] is directly relevant to the present work because the experiment used the same fluid pair and a straight-channel PCHE pre-cooler configuration. The tested heat exchanger consisted of straight semicircular microchannels with a channel diameter of $2.0\ \text{mm}$, an active microchannel length of $295.2\ \text{mm}$, 10 hot plates, 10 cold plates, and 10 channels per plate, resulting in 100 hot-side and 100 cold-side channels arranged in counterflow. Liu et al. also reported that the microchannel region accounts for more than 95% of the total heat-transfer area, supporting

the use of a representative straight-channel core model for assessing the dominant thermal response of the PCHE core.

Four operating conditions were selected from the experimental cases reported by Liu et al. [11]. The imposed model inputs were the hot- and cold-side inlet temperatures, inlet pressures, and total mass flow rates. The total experimental mass flow rates were converted to per-channel values by dividing by the number of parallel channels. The same one-dimensional distributed formulation used later for the inlet-state maps was applied to all assessment cases. CO_2 and water properties were evaluated locally using CoolProp, so that the strong variation of sCO_2 thermophysical properties near the pseudo-critical region was retained.

The assessment is intentionally limited to quantities that are available from the experimental datasets. For the Liu et al. cases, only inlet and outlet temperatures are used. Therefore, the comparison demonstrates that the model reproduces the dominant component-level thermal response of the selected straight-channel PCHE operating points, but it does not constitute a full validation of local heat-transfer coefficients, port-to-port pressure losses, header losses, entrance and exit losses, or flow maldistribution among parallel channels. This limitation is important because the subsequent state maps include quantities such as straight-core pressure drop and mean overall heat-transfer coefficient, which were not independently validated against local measurements.

The outlet-temperature deviation and mean absolute error are defined as:

$$\Delta T = T_{\mathrm{sim}} - T_{\mathrm{exp}}, \qquad (26)$$

$$\mathrm{MAE} = \frac{1}{N}\sum_{i=1}^{N} \mid T_{\mathrm{sim},i} - T_{\mathrm{exp},i} \mid . \qquad (27)$$

Here, T_{sim} and T_{exp} are the simulated and experimental outlet temperatures, respectively, and N is the number of compared operating points. Temperature deviations are reported as simulated minus experimental values.

In addition to the outlet-temperature comparison, the model was checked against the near-critical temperature profiles reported by Park et al. [10]. Park et al. investigated a straight-channel PCHE manufactured by photochemical etching and diffusion bonding for sCO_2 cooling with water. The selected case corresponds to a $640\ \mathrm{mm}$-long PCHE with $1.2\ \mathrm{mm}$ channel width, $1.2\ \mathrm{mm}$ plate thickness, and a CO_2-side pressure of $7.5\ \mathrm{MPa}$. This operating condition is particularly useful for the present study because the CO_2 stream is cooled from a gas-like supercritical state toward a liquid-like supercritical state near the critical region, where strong property variation makes the prediction of the axial temperature trajectory challenging.

For this comparison, the temperature profiles of both CO_2 and water were digitized from the reported Park et al. data. The mass flow rate required by the one-dimensional model was not explicitly available for the selected plotted temperature-profile case and was therefore inferred from the available thermal response. Consequently, this comparison should not be interpreted as an independent validation of the mass-flow dependence or as a strict predictive validation case.

Instead, it is used to examine whether the distributed model can reproduce the measured axial cooling and heating profile shapes once a physically consistent flow condition is imposed.

Figure 2 shows that the model captures the main qualitative features of the near-critical case: the rapid initial decrease in the CO_2 bulk temperature, the gradual approach of the CO_2 stream toward the near-critical outlet region, and the counterflow water-temperature rise. This comparison is useful because outlet-temperature agreement alone does not guarantee that the internal temperature trajectory is physically consistent. The remaining deviations are attributed to uncertainty in digitizing the experimental profiles, uncertainty in the inferred mass flow rate, possible differences between nominal and actual PCHE geometry, unmodeled axial conduction and header effects, and the known sensitivity of near-critical sCO_2 heat transfer to local wall temperature and property gradients.

The influence of the heat-transfer closure was also examined during the model-assessment stage. Several available sCO_2-side correlations were tested while keeping the same geometry, mass flow rates, and real-fluid property evaluation. The Ren et al. [7] correlation was retained because it gave the most consistent agreement with the available outlet-temperature and profile data without modifying the published empirical coefficients. Therefore, the selected correlation should be interpreted as a model-closure choice rather than as a new correlation development.

Quantity	**Case 1**	**Case 2**	**Case 3**	**Case 4**
CO_2 mass flow rate [kg h^{-1}]	130	110.6	115.7	85.7
$T_{h,in}$[K]	312.8	318.7	313.7	312.0
$T_{h,out}$, exp. [K]	307.9	311.0	311.3	307.7
$T_{h,out}$, sim. [K]	308.5	311.3	310.5	306.4
ΔT_h[K]	0.6	0.3	-0.8	-0.7
Water mass flow rate [kg h^{-1}]	217.9	207.5	84.9	84.7
$T_{c,in}$[K]	297.5	297.5	298.5	298.5
$T_{c,out}$, exp. [K]	304.9	307.1	308.1	306.4
$T_{c,out}$, sim. [K]	304.6	306.1	310.6	307.7
ΔT_c[K]	-0.3	-1.0	2.5	1.3

Table 1. Validation cases and outlet-temperature comparison.

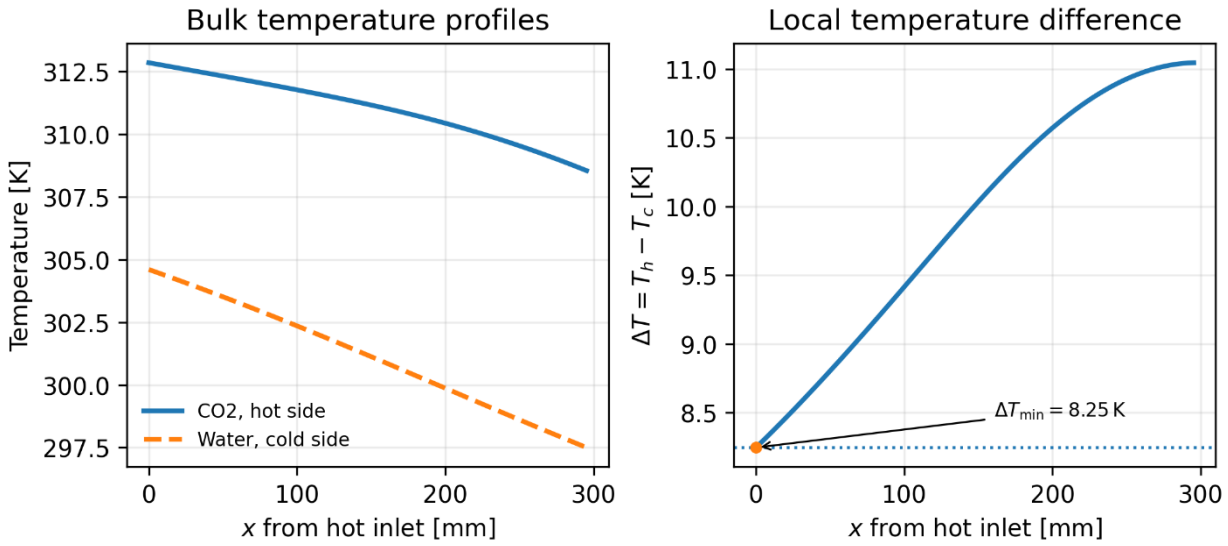

Fig. 1. Simulated bulk-temperature profiles and local temperature difference for validation Case 1. The local temperature difference remains positive throughout the exchanger, with $\Delta T_{min} = 8.25$ K occurring near the hot-side inlet.

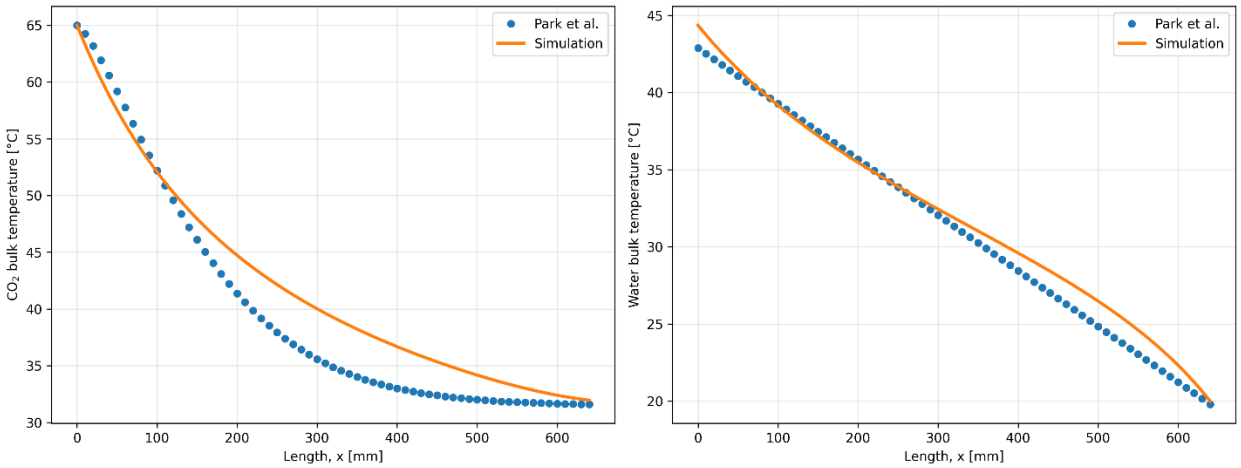

Fig. 2. Comparison between digitized experimental temperature profiles from Park et al. [10] and the present one-dimensional simulation for a near-critical sCO_2-water straight-channel PCHE case. The PCHE length is $L = 640\ mm$, the channel width is 1.2 mm, the plate thickness is 1.2 mm, and the CO_2-side pressure is 7.5 MPa. The axial coordinate is measured from the CO_2 inlet to the CO_2 outlet; therefore, the water-side profile is shown in the opposite flow direction. The mass flow rate was not explicitly reported for this plotted case and was evaluated from the available thermal response.

The sensitivity study shows whether the qualitative state-map structure is preserved when the hot-side heat-transfer closure is changed. In the present work, the correlation sensitivity is used to bound the uncertainty associated with the empirical heat-transfer closure. The resulting state maps should therefore be interpreted primarily as design-oriented sensitivity trends for the selected

geometry and model assumptions, rather than as universal quantitative predictions independent of correlation choice.

The wall-conduction model used in Eq. (10) includes a dimensionless conduction shape factor, S. This value was not treated as a fitting parameter. It was obtained from a separate two-dimensional unit-cell conduction calculation for the same semicircular-channel geometry and plate spacing used in the baseline model. For the baseline geometry, $D_{\mathrm{ch}} = 1.2\ \mathrm{mm}$, $t_{\mathrm{plate}} = 1.2\ \mathrm{mm}$, and $p = 1.8\ \mathrm{mm}$, the resulting value was $S = 1.406$.

An axial-resolution independence check was performed for a representative near-critical operating condition by varying the number of axial post-processing locations from $N_x = 50$ to $N_x = 500$. The outlet temperatures, heat duty, integrated conductance, minimum temperature approach, and hot-side straight-core pressure drop were unchanged to the reported precision. Therefore, $N_x = 300$ was used in the assessment cases and in the parametric state maps.

The pressure drops reported in this work correspond to the straight-channel core only. They represent the frictional contribution of the modeled heat-transfer passages and do not include inlet and outlet headers, manifolds, distributors, bends, contractions, expansions, port regions, or flow maldistribution. This distinction is important because, in an actual PCHE module, header and port losses may be comparable to or larger than the straight-core loss, especially when the predicted core pressure drop is below approximately $1\ \mathrm{kPa}$. Therefore, the pressure-drop maps presented later should be interpreted as comparative core-level hydraulic trends rather than as final module-level pressure-drop predictions.

Overall, the model assessment indicates that the one-dimensional distributed formulation provides adequate thermal accuracy for preliminary design-oriented inlet-state mapping. The Liu et al. comparison confirms that the model reproduces the component-level outlet-temperature response for selected straight-channel PCHE cases. The Park et al. comparison provides additional support that the model captures the qualitative axial temperature evolution in a near-critical sCO_2-water cooling process under an inferred flow condition. Nevertheless, the model should be interpreted as a straight-core thermal mapping tool, not as a fully validated component-level design code.

4. State-map methodology

A two-dimensional inlet-state mapping procedure was used to evaluate the sensitivity of the PCHE pre-cooler to the thermodynamic state of the incoming sCO_2. The hot-side inlet pressure, $p_{h,\mathrm{in}}$, and the hot-side inlet temperature, $T_{h,\mathrm{in}}$, were varied over the prescribed operating range, while the exchanger geometry, wall material, channel count, and mass flow rates were kept fixed. The cold-side fluid was water. Three cooling-water inlet temperatures were considered: 24 °C, 27 °C, and 30 °C.

For each point in the $p_{h,\mathrm{in}} - T_{h,\mathrm{in}}$ plane, the distributed one-dimensional model was solved and the axial profiles of temperature, pressure, enthalpy, local heat-transfer coefficient, and overall conductance were obtained. The following quantities were then extracted from the converged solution: total heat duty, effectiveness, hot-side straight-core pressure drop, cold-side straight-core pressure drop, outlet temperatures, minimum temperature approach, integrated conductance, and

mean overall heat-transfer coefficient. Each map point was solved using the same numerical procedure and model closures used in the validation cases.

Parameter	Value
Wall material	316L stainless steel
Channel diameter, D	2.0 mm
Channel length, L	295.2 mm
Channels per plate	10
Number of hot plates / cold plates	10 / 10
Plate thickness	1.6 mm
Channel pitch	3.0 mm
Hot-side mass flow rate	130 kg h^{-1}
Cold-side mass flow rate	217.91 kg h^{-1}
Hot-side inlet-pressure range	8.38-9.18 MPa
Hot-side inlet-temperature range	33.85-45.85 °C
Cold-side inlet temperatures	24, 27, and 30 °C

Table 2. Fixed geometry and operating parameters for state-map calculations.

The geometry corresponds to the straight semicircular-channel PCHE pre-cooler configuration used in the validation case. Only $p_{h,\mathrm{in}}$, $T_{h,\mathrm{in}}$, and the cooling-water inlet temperature are varied in the state maps. The reported pressure drops correspond to the modeled straight-channel core only and do not include header, manifold, port, entrance, exit, or flow-maldistribution losses.

4.1. Pseudo-critical line

The CO_2 pseudo-critical line was superimposed on each state map to relate the calculated pre-cooler response to the inlet thermodynamic state. For pressures above the critical pressure, the pseudo-critical temperature is commonly identified as the temperature at which the isobaric specific heat reaches its maximum along an isobar. In this work, the pseudo-critical temperature was evaluated using the pressure-dependent relation reported by Liao and Zhao [19],

$$T_{\mathrm{pc}} = -122.6 + 6.124p - 0.1657p^2 + 0.01773p^{2.5} - 0.0005608p^3, \qquad (28)$$

where T_{pc} is in °C and p is in bar. The considered pressure range, 8.38-9.18 MPa, is above the critical pressure of CO_2.

The lower-temperature side of the pseudo-critical line is described as liquid-like supercritical CO_2, while the higher-temperature side is described as gas-like supercritical CO_2. This classification is used only to interpret the inlet state. The distributed thermal path inside the exchanger may approach or cross the pseudo-critical region even when the inlet state is not located directly on the pseudo-critical line.

For strict consistency with the property package, the pseudo-critical line could also be evaluated directly from the maximum of $c_p(T, p)$using the same equation of state used in the solver. The polynomial form in Eq. (28) is retained here for consistency with the cited experimental heat-transfer literature and for ease of plotting.

5. Results and discussion

Figures 3-5 present the state-map results for cooling-water inlet temperatures of 24 °C, 27 °C, and 30 °C, respectively. In each figure, the hot-side inlet temperature, $T_{h,\mathrm{in}}$, and hot-side inlet pressure, $p_{h,\mathrm{in}}$, are varied while the geometry, channel count, wall material, and mass flow rates remain fixed. The dashed curve denotes the CO_2 pseudo-critical line. The six panels in each figure show heat duty, effectiveness, hot-side straight-core pressure drop, mean overall heat-transfer coefficient, minimum temperature approach, and hot outlet temperature.

5.1. Heat duty and active-core power density

The heat-duty maps show a strong dependence on hot-side inlet temperature. For all three water inlet temperatures, the heat duty increases as $T_{h,\mathrm{in}}$increases. This trend is expected because a higher CO_2 inlet temperature increases the available thermal driving force between the hot CO_2 and the cooling water. Within the mapped range, the largest heat duties occur in the higher-temperature, gas-like inlet region relative to the pseudo-critical line.

The cooling-water inlet temperature also has a first-order influence on the absolute cooling capacity. Increasing the cooling-water inlet temperature from 24 °C to 30 °C reduces the heat duty across the mapped domain. From the plotted ranges, the maximum heat duty decreases from approximately 2.0 kW at $T_{c,\mathrm{in}} = 24^{\circ}\mathrm{C}$ to approximately 1.5 kW at $T_{c,\mathrm{in}} = 30^{\circ}\mathrm{C}$ for the fixed geometry and flow rates. Because the active core volume is unchanged, the active-core power density follows the same spatial trend as the heat duty.

5.2. Effectiveness and heat-duty trade-off

The effectiveness maps show a trend that is distinct from the heat-duty maps. Although heat duty increases with $T_{h,\mathrm{in}}$, effectiveness generally decreases as $T_{h,\mathrm{in}}$ increases. The highest effectiveness values occur at lower hot-side inlet temperatures, especially toward the higher-pressure and more liquid-like part of the mapped range. Conversely, the lowest effectiveness values occur in the high-temperature, lower-pressure gas-like region.

This behavior reflects the difference between absolute heat removal and utilization of the maximum available thermal potential. At higher $T_{h,\mathrm{in}}$, the available enthalpy difference increases substantially. The exchanger removes more heat in absolute terms, but not in direct proportion to this larger ideal enthalpy potential. Consequently, the operating condition that maximizes heat duty does not also

maximize effectiveness. The maximum effectiveness decreases from about 0.61 for $T_{c,\mathrm{in}} = 24^{\circ}\mathrm{C}$, to about 0.58 for $T_{c,\mathrm{in}} = 27^{\circ}\mathrm{C}$, and to about 0.55 for $T_{c,\mathrm{in}} = 30^{\circ}\mathrm{C}$.

5.3. Hot-side straight-core pressure drop

The hot-side straight-core pressure drop increases toward higher $T_{h,\mathrm{in}}$ and lower $p_{h,\mathrm{in}}$. This trend is consistent with the thermodynamic transition toward lower-density, gas-like supercritical CO_2. For a fixed mass flow rate and channel geometry, lower density increases velocity and therefore increases the frictional pressure loss.

The predicted pressure drops are small, approximately 0.33 - 0.56 kPa over the plotted range, because only the modeled straight-channel core losses are included. These values should not be compared directly with full port-to-port experimental pressure drops unless header, manifold, inlet contraction, outlet expansion, and possible maldistribution losses are added.

5.4. Mean overall heat-transfer coefficient and pseudo-critical enhancement

The mean overall heat-transfer coefficient exhibits one of the clearest pseudo-critical signatures in the state maps. Unlike heat duty, $\bar{U}$ does not simply increase with $T_{h,\mathrm{in}}$. Instead, a ridge of high $\bar{U}$appears near the pseudo-critical line in all three cooling-water cases. This behavior is consistent with the strong variation of CO_2 properties near the pseudo-critical region.

The ridge in $\bar{U}$ does not exactly coincide with the pseudo-critical line. This is expected because the dashed line is defined from the inlet pressure and inlet temperature only, whereas $\bar{U}$is an integral quantity accumulated over the full channel length. During cooling, the CO_2 stream may approach or cross the pseudo-critical region inside the exchanger even if the inlet state is offset from the line. The peak values of $\bar{U}$ remain broadly similar among the three water inlet temperatures, with maxima of approximately 1.27-1.31 kW $\mathrm{m}^{-2}\ \mathrm{K}^{-1}$. Because local heat-transfer coefficients were not validated directly, this conclusion should be interpreted as a model-based indication rather than as an experimental demonstration of the exact magnitude of enhancement.

5.5. Minimum temperature approach and pinch margin

The minimum temperature approach, ΔT_{min}, provides a compact measure of pinch margin and thermal feasibility. The maps show that ΔT_{min} is strongly affected by the cooling-water inlet temperature. The smallest values in the mapped domain are approximately 5.2 K, 3.1 K, and 1.0 K for cooling-water inlet temperatures of 24 °C, 27 °C, and 30 °C, respectively. Thus, increasing the cooling-water inlet temperature moves the exchanger closer to a pinch-limited condition.

This result is important for operation under off-design heat-sink conditions. A warmer heat sink not only reduces total heat duty, it also reduces the minimum local thermal driving force and thereby reduces thermal margin. As $T_{h,\mathrm{in}}$ increases, ΔT_{min} increases because the available temperature difference is larger. Nevertheless, high $T_{h,\mathrm{in}}$ is not universally preferable because it also corresponds to lower effectiveness and higher hot-side core pressure drop.

5.6. Hot outlet temperature and pre-cooler objective

The hot outlet temperature, $T_{h,\mathrm{out}}$, is a central pre-cooler metric because it determines the CO_2 state delivered toward the compressor inlet. The maps show that $T_{h,\mathrm{out}}$ increases with $T_{h,\mathrm{in}}$, as expected, and is shifted upward when $T_{c,\mathrm{in}}$ increases. For $T_{c,\mathrm{in}} = 24^{\circ}\mathrm{C}$, the predicted hot outlet temperature ranges approximately from 28.3 °C to 38.3 °C. For $T_{c,\mathrm{in}} = 27^{\circ}\mathrm{C}$, the range increases to approximately 30.1-39.3 °C, and for $T_{c,\mathrm{in}} = 30^{\circ}\mathrm{C}$, it increases further to approximately 31.8-40.1 °C.

The same fixed PCHE core can therefore deliver substantially different compressor-inlet thermal conditions depending on the available cooling-water temperature. Lower water inlet temperature allows the exchanger to cool the CO_2 further into the lower-temperature, more liquid-like region. Warmer water reduces this capability and leaves a larger portion of the mapped outlet states closer to the pseudo-critical or gas-like side.

5.7. Design interpretation

The state maps reveal a multi-objective trade-off. Higher $T_{h,\mathrm{in}}$ increases heat duty and active-core power density, but it also tends to reduce effectiveness and increase hot-side straight-core pressure drop. Higher pressure generally reduces the pressure-drop penalty and shifts the pseudo-critical line to higher temperature. Lower cooling-water inlet temperature improves heat duty, effectiveness, pinch margin, and hot outlet temperature simultaneously.

The most useful operating region is therefore not necessarily the region of maximum heat duty. For pre-cooler design, the preferred envelope should satisfy multiple constraints simultaneously: sufficient heat removal, acceptable compressor-inlet temperature, adequate minimum temperature approach, favorable pseudo-critical heat-transfer behavior, and acceptable pressure loss. The proposed state-map representation provides a compact way to visualize these competing effects. Its role is preliminary screening and operating-point interpretation; final design should include a full component pressure-drop model, manifold effects, manufacturing constraints, and validation over a broader set of near-critical operating conditions.

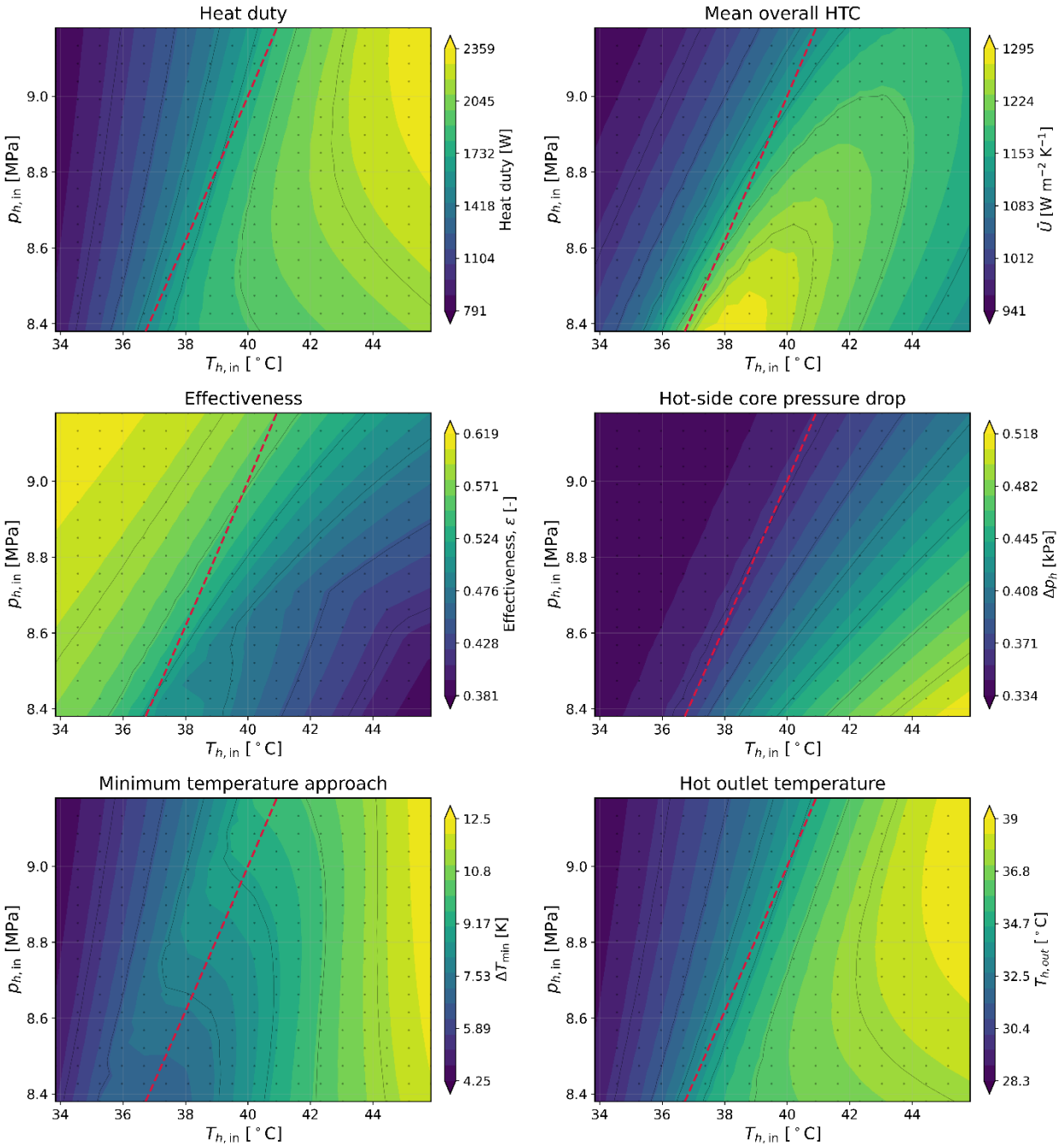

Fig. 3. State-map results for the PCHE pre-cooler at $T_{c,in} = 24$°C. The six panels show heat duty, effectiveness, hot-side straight-core pressure drop, mean overall heat-transfer coefficient, minimum temperature approach, and hot outlet temperature as functions of $T_{h,in}$ and $p_{h,in}$.

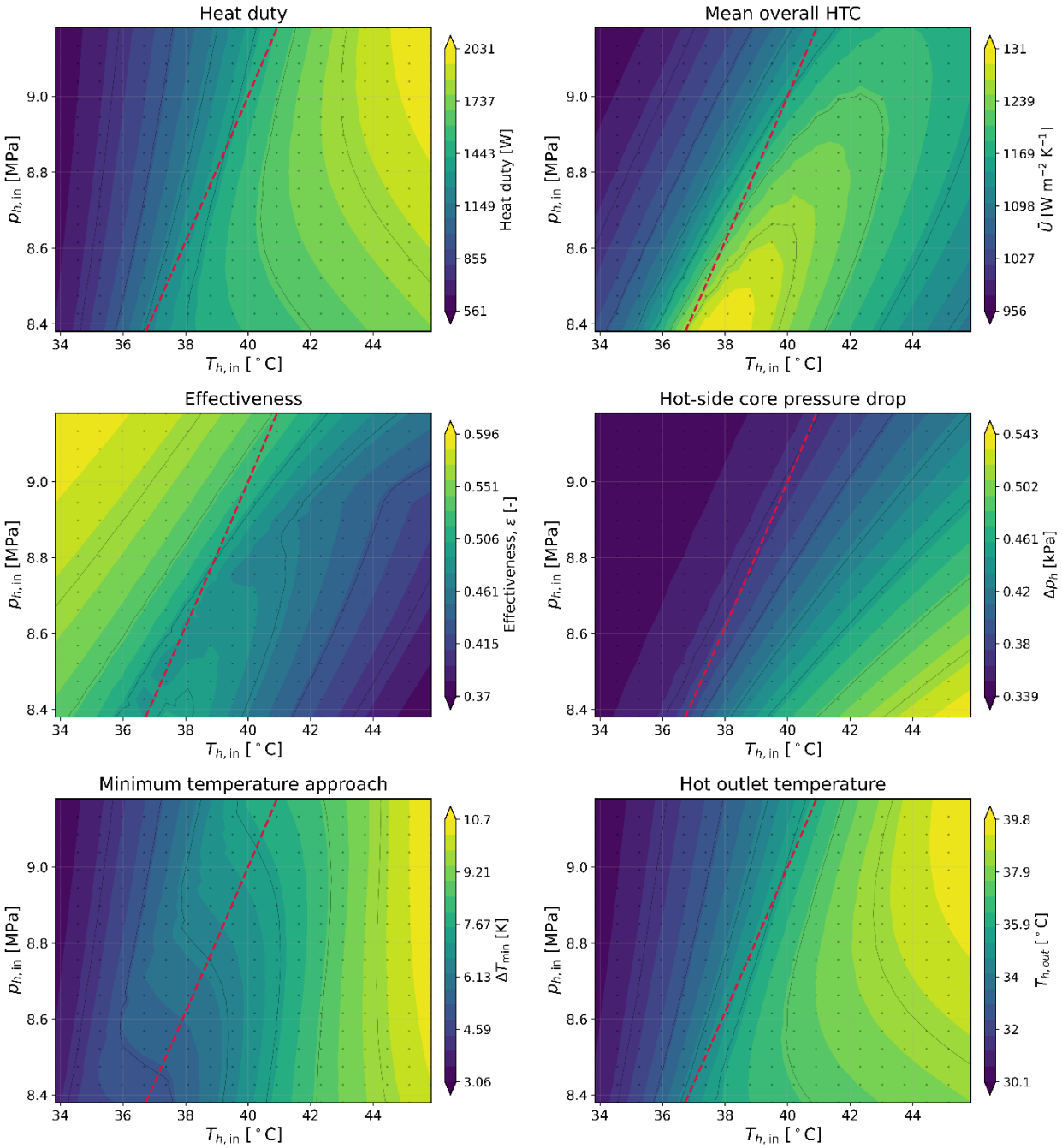

Fig. 4. State-map results for the PCHE pre-cooler at $T_{c,in} = 27$°C. Compared with the 24 °C case, heat duty, effectiveness, and pinch margin are reduced, while hot outlet temperature is shifted upward.

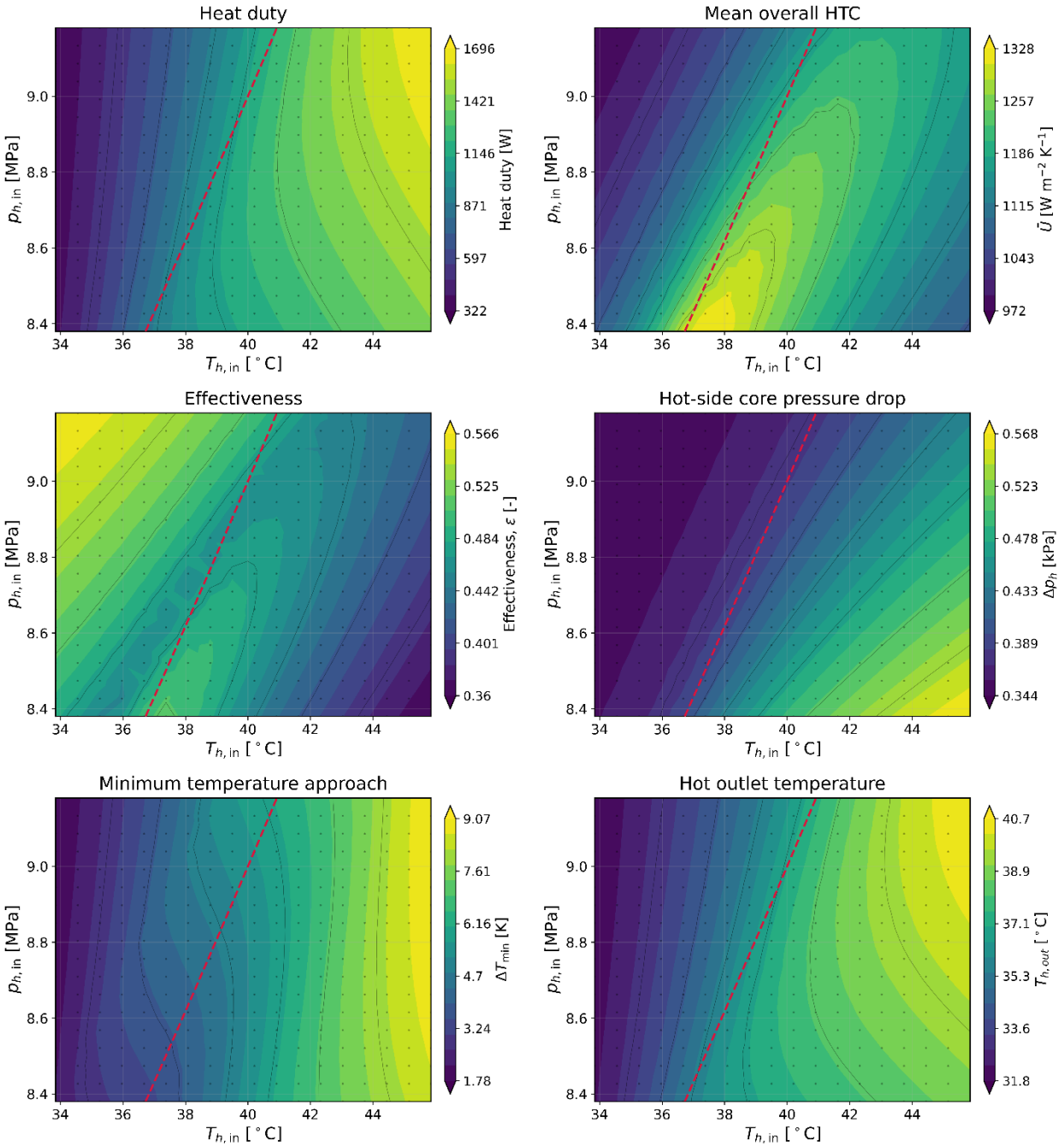

Fig. 5. State-map results for the PCHE pre-cooler at $T_{c,in} = 30$°C. This warmest-water case gives the lowest heat duty, lowest effectiveness, smallest minimum temperature approach, and highest hot outlet temperature among the three cases considered.

6. Conclusions

A one-dimensional distributed model was developed and applied to construct pseudo-critical inlet-state maps for an sCO_2-water printed circuit heat exchanger pre-cooler. The model was assessed against two types of available experimental information: outlet-temperature data from Liu et al. and digitized near-critical axial temperature profiles from Park et al. For the selected Liu et al. cases, the model reproduced the reported outlet temperatures with a mean absolute error of approximately $0.6\ \mathrm{K}$ for the CO_2 outlet temperature and $1.28\ \mathrm{K}$ for the water outlet temperature. The comparison with the Park et al. profiles showed that the model captures the qualitative axial cooling trend of CO_2 and the counterflow heating trend of water near the critical region. However, because the mass flow rate corresponding to the selected Park et al. plotted profile was not explicitly available and was inferred from the thermal response, this comparison should be interpreted as a profile-shape consistency check rather than as a fully independent predictive validation case.

The state maps demonstrate that the response of a fixed PCHE pre-cooler core cannot be characterized by heat duty alone. Heat duty increases mainly with increasing $T_{h,\mathrm{in}}$ and decreasing $T_{c,\mathrm{in}}$, whereas effectiveness follows a competing trend because the available enthalpy potential increases faster than the heat removed. The hot-side straight-core pressure drop increases toward higher $T_{h,\mathrm{in}}$ and lower $p_{h,\mathrm{in}}$, where the CO_2 density is lower and the velocity is higher for the fixed mass flow rate and channel geometry. The mean overall heat-transfer coefficient, $\bar{U}$, exhibits a ridge near the pseudo-critical line, indicating that, within the selected heat-transfer closure, the strongest intrinsic heat-transfer enhancement occurs when the distributed CO_2 cooling path approaches the pseudo-critical region. The minimum temperature approach, $\Delta T_{\min}$, is strongly affected by the cooling-water inlet temperature; increasing $T_{c,\mathrm{in}}$ reduces the pinch margin and moves the exchanger closer to a thermally constrained operating condition. The hot outlet temperature also increases with both $T_{h,\mathrm{in}}$ and $T_{c,\mathrm{in}}$, confirming that heat-sink temperature is a first-order off-design parameter for compressor-inlet temperature control.

The main contribution of the study is therefore the state-map interpretation rather than the development of a new local heat-transfer model. By combining distributed real-fluid calculations with a two-dimensional $p_{h,\mathrm{in}} - T_{h,\mathrm{in}}$ representation, the method provides a compact preliminary design tool for identifying operating regions that balance cooling capacity, effectiveness, pseudo-critical heat-transfer enhancement, pinch margin, outlet temperature, and straight-core hydraulic penalty. This type of representation is useful because the preferred operating envelope is not necessarily located at the maximum heat duty or maximum heat-transfer coefficient; it depends on simultaneous thermal and hydraulic constraints relevant to sCO_2 Brayton-cycle pre-cooler operation.

The results should be interpreted as straight-core trends for the specified geometry, real-fluid property model, and selected empirical closures. The reported pressure drops do not include headers, manifolds, port losses, inlet and outlet losses, or flow maldistribution, and the local heat-transfer coefficients were not independently validated against local measurements. Future work should therefore include broader experimental validation, direct pressure-drop comparison, explicit treatment of manifold and port losses, flow-maldistribution modeling, axial-conduction assessment, and component-level or CFD-based verification. A broader heat-transfer-correlation sensitivity study is also recommended, since the absolute magnitudes of $\bar{U}$, heat duty, and outlet

temperature can depend on the selected sCO_2-side closure, even when the qualitative structure of the state maps is preserved.

Data Availability Statement

The datasets generated and analyzed during the current study are available from the corresponding author upon reasonable request. Experimental validation data used for comparison were obtained from the cited literature.

Statements & Declarations

Funding
The author declares that no funds, grants, or other support were received during the preparation of this manuscript.

Competing Interests
The author declares that he has no competing interests.

References

[1] Dostal V, Driscoll MJ, Hejzlar P (2004) A supercritical carbon dioxide cycle for next generation nuclear reactors. MIT-ANP-TR-100, Massachusetts Institute of Technology, Cambridge, MA

[2] Sarkar J (2009) Second law analysis of supercritical CO_2 recompression Brayton cycle. Energy 34:1172–1178. https://doi.org/10.1016/j.energy.2009.04.030

[3] Kwon JS, Son S, Heo JY, Lee JI (2020) Compact heat exchangers for supercritical CO_2 power cycle application. Energy Conversion and Management 209:112666. https://doi.org/10.1016/j.enconman.2020.112666

[4] Chai L, Tassou SA (2020) A review of printed circuit heat exchangers for helium and supercritical CO_2 Brayton cycles. Thermal Science and Engineering Progress 18:100543. https://doi.org/10.1016/j.tsep.2020.100543

[5] Ma Y, Liu D, Wang J, Zeng M, Wang Q, Ma T (2025) Thermal-hydraulic performance and optimization of printed circuit heat exchangers for supercritical fluids: A review. Renewable and Sustainable Energy Reviews 208:115051. https://doi.org/10.1016/j.rser.2024.115051

[6] Chu WX, Li XH, Ma T, Chen YT, Wang QW (2017) Experimental investigation on SCO_2–water heat transfer characteristics in a printed circuit heat exchanger with straight channels. International Journal of Heat and Mass Transfer 113:184–194. https://doi.org/10.1016/j.ijheatmasstransfer.2017.05.059

[7] Ren Z, Zhao CR, Jiang PX, Bo HL (2019) Investigation on local convection heat transfer of supercritical CO_2 during cooling in horizontal semicircular channels of printed circuit heat exchanger. Applied Thermal Engineering 157:113697.

https://doi.org/10.1016/j.applthermaleng.2019.04.107

[8] Li XH, Deng TR, Ma T, Ke HB, Wang QW (2019) A new evaluation method for overall heat transfer performance of supercritical carbon dioxide in a printed circuit heat exchanger. Energy Conversion and Management 193:99–105. https://doi.org/10.1016/j.enconman.2019.04.061

[9] Cheng K, Zhou J, Zhang H, Huai X, Guo J (2020) Experimental investigation of thermal-hydraulic characteristics of a printed circuit heat exchanger used as a pre-cooler for the supercritical CO_2 Brayton cycle. Applied Thermal Engineering 171:115116. https://doi.org/10.1016/j.applthermaleng.2020.115116

[10] Park JH, Kwon JG, Kim TH, Kim MH, Cha JE, Jo H (2020) Experimental study of a straight channel printed circuit heat exchanger on supercritical CO_2 near the critical point with water cooling. International Journal of Heat and Mass Transfer 150:119364. https://doi.org/10.1016/j.ijheatmasstransfer.2020.119364

[11] Liu B, Lu M, Shui B, Sun Y, Wei W (2022) Thermal-hydraulic performance analysis of printed circuit heat exchanger precooler in the Brayton cycle for supercritical CO_2 waste heat recovery. Applied Energy 305:117923. https://doi.org/10.1016/j.apenergy.2021.117923

[12] Jin F, Yuan D, Chen D, Hu L, Huang Y, Bu S (2023) Experimental study on cooling heat transfer performance of supercritical CO_2 in zigzag printed circuit heat exchanger. International Journal of Heat and Mass Transfer 215:124538. https://doi.org/10.1016/j.ijheatmasstransfer.2023.124538

[13] Wu D, Wei M, Tian R, Zheng S, He J (2022) A review of flow and heat transfer characteristics of supercritical carbon dioxide under cooling conditions in energy and power systems. Energies 15:8785. https://doi.org/10.3390/en15238785

[14] Bell IH, Wronski J, Quoilin S, Lemort V (2014) Pure and pseudo-pure fluid thermophysical property evaluation and the open-source thermophysical property library CoolProp. Industrial & Engineering Chemistry Research 53(6):2498–2508. https://doi.org/10.1021/ie4033999

[15] Span R, Wagner W (1996) A new equation of state for carbon dioxide covering the fluid region from the triple-point temperature to 1100 K at pressures up to 800 MPa. Journal of Physical and Chemical Reference Data 25(6):1509–1596. https://doi.org/10.1063/1.555991

[16] Gnielinski V (1976) New equations for heat and mass transfer in turbulent pipe and channel flow. International Chemical Engineering 16:359–368

[17] Petukhov BS (1970) Heat transfer and friction in turbulent pipe flow with variable physical properties. Advances in Heat Transfer 6:503–564

[18] Filonenko N (1954) Hydraulic resistance in pipes. Teploenergetika 1 :40–44

[19] Liao SM, Zhao TS (2002) Measurements of heat transfer coefficients from supercritical carbon dioxide flowing in horizontal mini/micro channels. Journal of Heat Transfer 124(3):413–420. https://doi.org/10.1115/1.1423906